LA-6257

C.3

UC-34c
Reporting Date: February 1976
Issued: August 1976

Double-Differential Beryllium Neutron Cross Sections at Incident Neutron Energies of 5.9, 10.1, and 14.2 MeV

by

Darrell M. Drake
George F. Auchampaugh
Edward D. Arthur
Charles E. Ragan
Phillip G. Young

los alamos
scientific laboratory
of the University of California
LOS ALAMOS, NEW MEXICO 87545

UNITED STATES
ENERGY RESEARCH AND DEVELOPMENT ADMINISTRATION
CONTRACT W-7405-ENG. 36

Printed in the United States of America. Available from
National Technical Information Service
U.S. Department of Commerce
5285 Port Royal Road
Springfield, VA 22161
Price: Printed Copy $3.50 Microfiche $2.25

DOUBLE-DIFFERENTIAL BERYLLIUM NEUTRON CROSS SECTIONS AT INCIDENT NEUTRON ENERGIES OF 5.9, 10.1, AND 14.2 MeV

by

**Darrell M. Drake, George F. Auchampaugh, Edward D. Arthur,
Charles E. Ragan, and Phillip G. Young**

ABSTRACT

We measured beryllium neutron-production cross sections using the time-of-flight technique at incident neutron energies of 5.9, 10.1, and 14.2 MeV, and at laboratory angles of 25°, 27.5°, 30°, 35°, 45°, 60°, 80°, 100°, 110°, 125°, and 145°. The differential elastic and inelastic cross sections are presented. Inelastic is defined here as those reactions that proceed through the states at 1.69-, 2.43-, 2.8-, and 3.06-MeV excitation energy in ^{9}Be. Comparison of our emission energy spectra with calculations using the ENDF/B-IV beryllium cross sections shows that the ENDF/B cross sections strongly overemphasize the low-lying states in ^{9}Be.

I. INTRODUCTION

Beryllium has been proposed as a major constituent of controlled fusion reactors because of its unique characteristic of emitting two neutrons for each inelastic neutron interaction. These neutrons can be used to produce tritium, one of the major fuel components of the reactor. Calculating the tritium breeding rate in proposed reactor vessel walls requires detailed knowledge of the energies and angular distributions of the neutrons emitted from beryllium under bombardment by energetic neutrons. Almost no such information is available for beryllium, especially for the (n,2n) reaction. Therefore, we measured the energies and angular distributions of the neutron emission spectra from beryllium at incident neutron energies of 5.9, 10.1, and 14.2 MeV.

II. EXPERIMENTAL DETAILS

A. Neutron Sources, General

To measure differential continuum cross sections, such as that for the beryllium (n,2n) reaction, with monoenergetic neutrons, it is desirable to choose a neutron source with a high yield of monoenergetic neutrons compared with background neutrons and with a background spectrum that can be measured. For gas targets the neutron background is produced primarily by charged particle reactions in the entrance foil and beam stop materials, and to a lesser extent by three-body breakup reactions in the gas. The background associated with the entrance foil and the beam stop materials can in principle be measured by removing the gas from the target cell and by measuring the resultant neutron flux.

However, neutrons produced in three-body breakup and subsequently scattered from the sample cannot be distinguished from those that are emitted by the scattering sample in reactions with the primary neutron beam. Therefore, source reactions that do not produce breakup neutrons in the incident neutron energy region of interest, are strongly preferred.

Several charged particle reactions are commonly used at the Los Alamos Scientific Laboratory (LASL) Van de Graaff accelerators to produce nearly monoenergetic neutron beams in the energy range studied. These are $^2H(d,n)^3He$, $^3H(p,n)^3He$, $^1H(t,n)^3He$, $^2H(t,n)^4He$, and $^3H(d,n)^4He$. The first two reactions, $^2H(d,n)^3He$ and $^3H(p,n)^3He$, have three-body breakup thresholds at 4.45- and 8.34-MeV incident particle energy, which correspond to primary neutron energies of 7.70 and 7.57 MeV, respectively. In addition, the breakup background from the $^2H(d,n)^3He$ reaction is much greater than that from the $^3H(p,n)^3He$ reaction. The $^1H(t,n)^3He$ reaction, because of the large center-of-mass energy, produces no breakup neutrons in the energy range of concern in this report. Furthermore, the primary neutron yield at 0° can be as much as 40 times that of the $^3H(p,n)^3He$ reaction for comparable resolution and incident beam current. Thus, in this experiment, being able to accelerate tritons and protons is a significant advantage. (For more details about monoenergetic neutron source reactions, associated backgrounds, and the influence of entrance foil and beam stop materials, see Ref. 1.) We also took data using the $^3H(p,n)^3He$ reaction to confirm our $^1H(t,n)^3He$ reaction data. The choice of whether to use the $^3H(d,n)^4He$ or the inverse reaction to produce 14-MeV neutrons was based on experimental considerations and will be discussed in more detail in Sec. II.C.

B. 6- and 10-MeV Neutron Sources

The tandem Van de Graaff was used to produce 5.9- and 10.1-MeV neutrons with the $^1H(t,n)^3He$ and $^3H(p,n)^3He$ reactions. The charged particle beam was bunched to a 1.5-ns pulse width by a klystron bunching system with a 1.25-MHz frequency.

The entrance foils to the target cell were either 5- or 10- mg/cm^2 molybdenum. The cell was filled to approximately 2.72 atm (40 psia) with either hydrogen or tritium gas. For both source reactions a gold beam stop was used. The calculated neutron energy spread from straggling of the tritons in the gas and from kinematic broadening was ± 120 keV for 6-MeV neutrons and ± 90 keV for 10-MeV neutrons. The energy spread for protons was substantially less.

The scattering samples were placed about 164 mm in front of the target cell at 0° to the charged particle beam direction. The distance from the neutron detector to the center of the sample was 2.70 m. The scattering angle was changed by rotating the neutron detector about the center of the sample.

C. 14.2-MeV Neutron Source

Monoenergetic 14-MeV neutrons can be produced by the $^2H(t,n)^4He$ or the inverse, $^3H(d,n)^4He$, reaction. We chose the $^2H(t,n)^4He$ reaction because there is somewhat less energy spread in the 90° neutron flux and because a cell filled with deuterium is less hazardous than one filled with tritium. The triton beam was chopped in the terminal of the vertical Van de Graaff accelerator to a pulse width of 10 ns at a frequency of 2 MHz and, after being accelerated to 2.5 MeV, was compressed to a pulse width of 1 ns by a Mobley buncher.[2] The beam passed through a 10-mg/cm^2 molybdenum foil and was stopped by the deuterium gas in the target cell.

The samples were placed in the plane perpendicular to the beam, where the average neutron energy was 14.2 MeV and the average kinematic energy spread was about ± 300 keV. The samples and detector were located about 150 mm above the horizontal beam plane. (See Fig. 1, Ref. 3.) The scattering angle was changed by rotating the sample about the beam axis. The detector was moved forward or backward as the angles were changed to keep the flight path constant at 2.77 m.

D. Samples

The beryllium, carbon, and polyethylene scattering samples were machined into right circular cylinders, 32-mm long by 32-mm o.d., with inside diameters of 0.5, 19.3, and 28.8 mm. The cylindrical axis was oriented perpendicular to the charged particle beam for the 5.9- and 10.1-MeV measurements and parallel to the beam for the 14.2-MeV measurements.

E. Neutron Detector

The neutron detector consisted of a 100-mm-diam by approximately 76-mm-thick Ne-213 liquid scintillator directly coupled to an RCA-8854 photomultiplier.[4] We noticed an improvement in the discrimination against gamma rays by eliminating the usual UV-Lucite coupling plate and placing the NE-213 scintillator in direct contact with the photomultiplier tube. The detector was placed in a large container made of copper, polyethylene, borated polyethylene, and lead and was shielded from the direct neutron source by a brass or tungsten shadow bar.

We set the detector bias near the pulse-height minimum between the 26- and 59-keV ^{241}Am gamma rays, which corresponds to a neutron energy of about 300 keV. The ^{241}Am source was mounted in a lead container near the side of the detector and could be remotely positioned, thereby allowing us to check the bias periodically.

A standard pulse-shape discrimination (PSD) circuit based upon the zero-crossover technique of Alexander and Goulding[5] was used to distinguish between neutron and gamma-ray pulses. This circuit had a pulse-height dynamic range of about 250:1, which permitted the entire secondary neutron energy range from 0.3 MeV to 16.7 MeV to be covered with one bias setting.

A plutonium-beryllium neutron source was periodically placed at a standard position near the neutron detector to check the stability of the PSD circuit. The drift in the PSD bias was negligible.

F. Electronics

The time-of-flight information was digitized into 1/8-ns time channels by an EG&G No. TDC-100 time digitizer. The digitizer was started by a pulse from a constant fraction discriminator that was fed by the anode pulse from the photomultiplier. The stop pulse originated from a beam sensor near the target. The data were stored in an XDS-930 computer in 1/2-ns time bins and transferred to magnetic tape for analysis on a CDC-7600 computer.

III. DATA REDUCTION

A. General

The number of neutrons detected with an efficiency $\epsilon(E')$ per MeV that are scattered from a sample of beryllium into a solid angle Ω is given by

$$A(E')=C(E')-B(E')\propto \phi(E)M_S(E;E',\Omega)n\Omega\varepsilon(E')\ \frac{d^2\sigma(E')}{dE'd\Omega}, \tag{1}$$

where $\phi(E)$ is the number of neutrons of energy E incident on the sample, n is the areal atom density of the sample, M_s is the correction for multiple scattering of neutrons of energy E into neutrons of energy E′ and solid angle Ω, B(E′) is the neutron background detected at the time corresponding to a neutron of energy E′, and C(E′) is the total number of neutrons detected. A similar expression can be written for a hydrogen sample with the same dimensions

$$\Sigma A_H(E) \propto \phi(E)M_S^H(E;E,\Omega)n^H\Omega\ \frac{d\sigma_H(E)}{d\Omega}\ \varepsilon(E), \tag{2}$$

where the sum extends over all channels that define the area of the hydrogen elastic peak. Solving for $\phi(E)$ in Eq. (2) and substituting it into Eq.(1) results in the following expression for the double-differential cross section

$$\frac{d^2\sigma(E)}{dE'd\Omega} = K(E)\ \frac{[C(E') - B(E')]}{\varepsilon_{rel}(E')M_S(E;E',\Omega)}\ . \tag{3}$$

The differential cross section is obtained by integrating Eq. (3) over the emission neutron energy E′. Because we are taking a ratio of two measurements, both using the same detector, only the relative efficiency of the detector is required for determining the cross section.

Polyethylene samples were used to obtain the hydrogen data. At small angles and high incident neutron energies the hydrogen elastic peak was not completely resolved from the carbon elastic and inelastic peaks. Therefore, data were taken with a carbon sample and used to correct the area of the hydrogen elastic peak. Many sets of polyethylene-carbon data were taken at each incident energy and for various angles to determine the constant K(E).

B. Relative Neutron Efficiency

The relative neutron efficiency of our detector was measured from 0.3 to 20 MeV using neutrons from the reactions $^2H(d,n)^3He$, $^3H(p,n)^3He$, $^3H(d,n)^4He$, and by elastically scattering neutrons from hydrogen. An efficiency plot is shown in Fig. 1. The various reactions used in each energy range are also indicated. The evaluations of Liskien and Paulsen[6] were used for the charged particle cross sections, and the hydrogen differential cross section[7] was taken from the ENDF/B-IV cross-section library. The peak at approximately 15 MeV in the efficiency curve is caused by the $^{12}C(n,n'3\alpha)$ reaction in the carbon of the scintillator and is visible only as a consequence of the low bias on our detector.

C. Multiple Scattering Correction

Multiple scattering corrections were calculated with the LASL Monte Carlo code MCN.[8] The geometry used in the calculations was an unshielded detector without a shadow bar and an isotropic monoenergetic neutron source. The scattered neutrons were tallied by energy and angle according to the type of reaction that created them: elastic, inelastic, elastic-elastic, elastic-inelastic, inelastic-inelastic, and the sum of all five processes. The calculations using MCN with various fictitious sample densities showed that spectra computed with a sample of 0.01 or less of normal density were not measurably distorted by the multiple neutron scattering processes. Therefore, to get M_s we ran MCN with a normal density sample and then repeated the calculation with a sample of one-hundredth normal density. The multiple scattering correction was obtained by taking a ratio of these two spectra for each angle multiplied by the atom density ratio for the two samples. Tables of M_s were generated for incident neutrons of energies 5.9, 10.1, and 14.2 MeV and for up to 20 values of emergent neutron energies. These tables were linearly interpolated to obtain the values of M_s used in computing the cross sections.

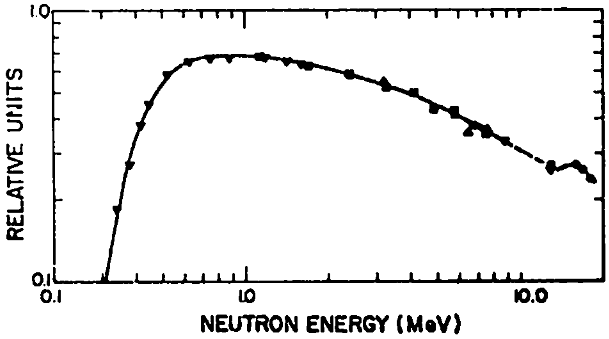

Fig. 1.

Relative efficiency of the neutron detector vs energy. Reactions used to obtain this curve were $^3H(p,n)^3He$ (▼), $^1H(n,n)^1H$ (■), $^3H(d,n)^4He$ (●), *and* $^2H(d,n)^3He$ (▲). *The increase in efficiency at approximately 15 MeV is from the* $^{12}C(n,n',3\alpha)$ *reaction in the carbon of the liquid scintillator.*

D. Background Sources

For the 5.9- and 10.1-MeV measurements the four sources of neutron background that need to be considered, particularly in the continuum region, are (1) breakup neutrons in the gas, which can be ignored for the $^1H(t,n)^3He$ reaction, (2) neutrons from the charged particle reactions in the foil and beam stop, (3) neutrons that scatter off the shadow bar into the sample and then rescatter into the detector, and (4) neutrons that scatter from the shield surrounding the detector. By taking the following four spectra at each incident energy and angle, most of the sources of background can be removed from the data. These are spectra with either hydrogen or tritium in the cell and the sample (a) in and (b) out, and spectra with either the hydrogen gas removed or the tritium gas replaced with helium gas and the sample (c) in or (d) out. A typical set of these four spectra for 10.1-MeV incident neutrons from the $^1H(t,n)^3He$ reaction at a 60° laboratory scattering angle is shown in Fig. 2. The spectra are combined by subtracting (b) from (a) and (d) from (c), and then subtracting the resulting two spectra. The final spectrum, however, still contains a background from neutrons that scatter off the shadow bar into the sample and then rescatter into the detector. Monte Carlo calculations show that the effect of the shadow bar on the spectrum is negligible.

For the $^3H(p,n)^3He$ reaction, the spectrum has an additional background from the tritium breakup process, which is present only in the continuum region. The yield from the $^3H(p,n)^3He$ reaction is also lower, giving poorer statistics on this data.

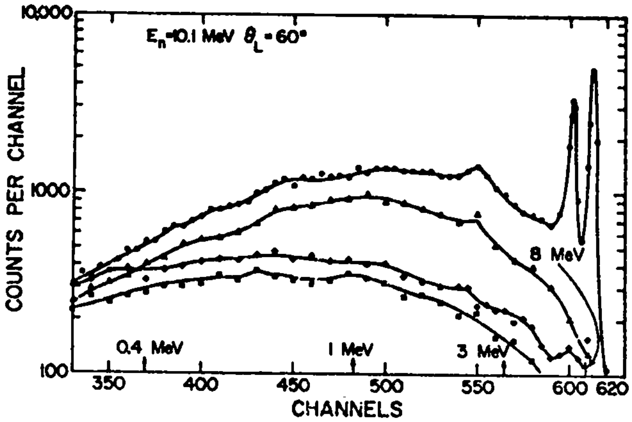

Fig. 2.

Time-of-flight spectra for 10.1-MeV incident neutrons on beryllium for a laboratory scattering angle of 60°. The source reaction is $^1H(t,n)^3He$ and the four spectra are: sample in - gas in (●), sample in - gas out (▲), sample out - gas in (♦), and sample out - gas out (■).

Therefore, only the elastic cross sections were determined from the data obtained using the $^3H(p,n)^3He$ reaction. The values were in good agreement with those obtained from the inverse reaction.

For the 14-MeV measurements, relatively few neutrons were produced by the low-energy tritons in the entrance foil, and the main source of neutron background was caused by less than ideal shielding of the detector from the direct 14-MeV neutrons. For this reason, only sample-in and sample-out data were taken at each angle for these measurements.

E. Data Code

A FORTRAN code was written to reduce the raw spectra to cross sections using Eq. (3). This code performed a channel by channel subtraction of the appropriate background spectra as outlined above, computed the relativistic energy and the relative efficiency for each channel, corrected for multiple scattering, and tabulated the cross section with statistical error (in mb/MeV·sr) in both the laboratory and the center-of-mass systems.

IV. RESULTS

The double-differential cross sections for 5.9-, 10.1-, and 14.2-MeV incident neutron energies are shown in Fig. 3. These cross sections are given in the laboratory system. The errors represent the statistical uncertainty of each data point. The energies of the low-lying levels in ^{9}Be are indicated with arrows. The first maximum below the elastic peak probably includes a contribution from the 1.68-MeV state in ^{9}Be. However, our energy resolution, except for the measurement at 5.9 MeV, is not sufficient to separate this contribution from that of other states nearby. For 5.9-MeV neutrons we see no branching to the 1.68-MeV state. The broadening at the base of the elastic peak for 5.9-MeV neutrons at an angle of 125° is due to improper bunching of the charged particle beam.

The differential elastic and inelastic cross sections corresponding to the 1.69-, 2.43-, 2.8-, and 3.06-MeV states in ^{9}Be (hereafter referred to collectively as the "2.43-MeV" state) for 5.9-, 10.1-, and 14.2-MeV incident neutrons are given in Table I. These cross sections were obtained by integrating the appropriate peaks in the energy distribution curves in Fig. 3. The errors given in Table I on each cross section represent a quadrature of the statistical and systematic errors. The systematic errors used at the three energies for the elastic cross sections were 13%, 13%, and 11%, respectively. These included uncertainties in the normalization constant (K), efficiency, multiple scattering, and, for the inelastic cross sections, an uncertainty in the definition of the peak area.

The cross sections for neutrons emitted to states above the "2.43-MeV" state, referred to as double-differential continuum cross sections, are given in Tables II-IV. For these cross sections the systematic uncertainty varied with energy and angle but averaged about 11%.

The cross sections presented in Tables I-IV are neutron production cross sections and therefore should be divided by the number of neutrons emitted in the reaction. For the elastic reaction this number is one, and for the inelastic reaction it is usually considered two because no gamma-ray emission from the excited states in ^{9}Be has been observed even at 14 MeV.[9] Inelastic scattering leaves the ^{9}Be nucleus in a state which preferentially decays by neutron emission.

The angle-integrated cross sections are given in Table V. These elastic and inelastic cross sections were obtained by using Wick's[10] inequality [$\sigma(0°) > (k\sigma_T/4\pi)^2$, where k is the center-of-mass wave number and σ_T is the total cross section] to extrapolate the elastic distribution to 0° and by using reasonable extrapolations to 0° and 180° for the

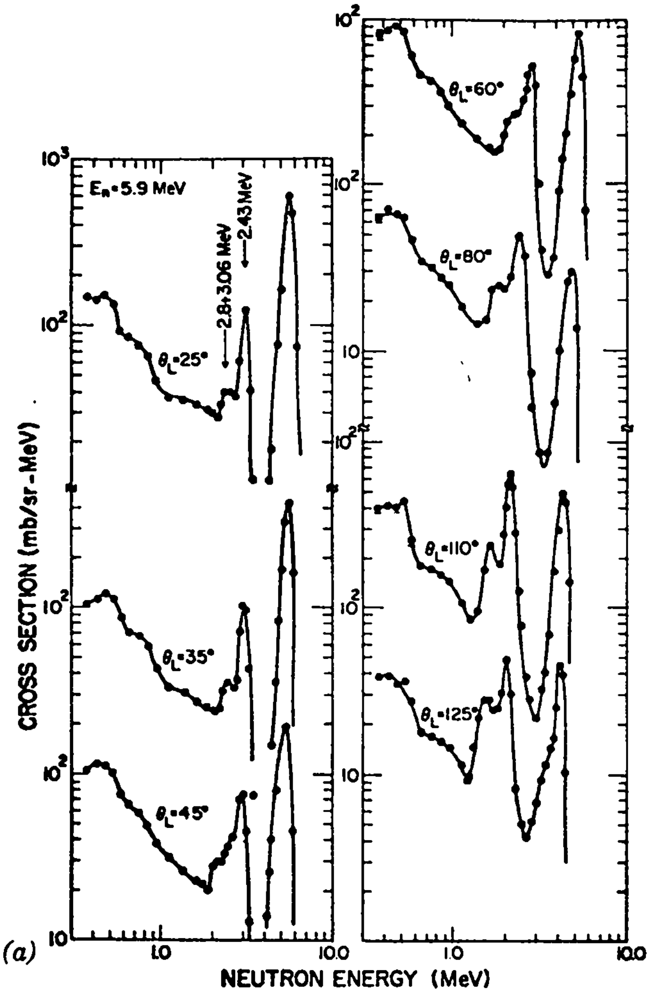

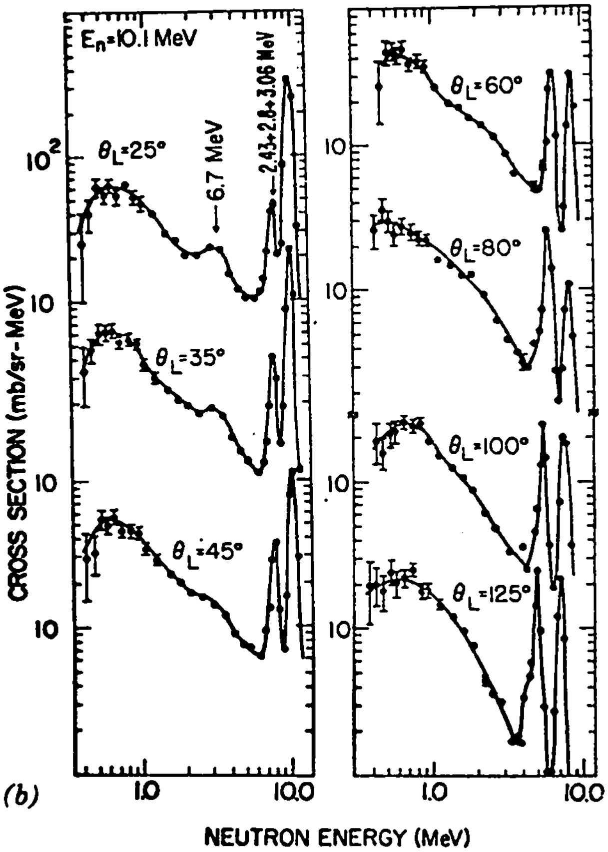

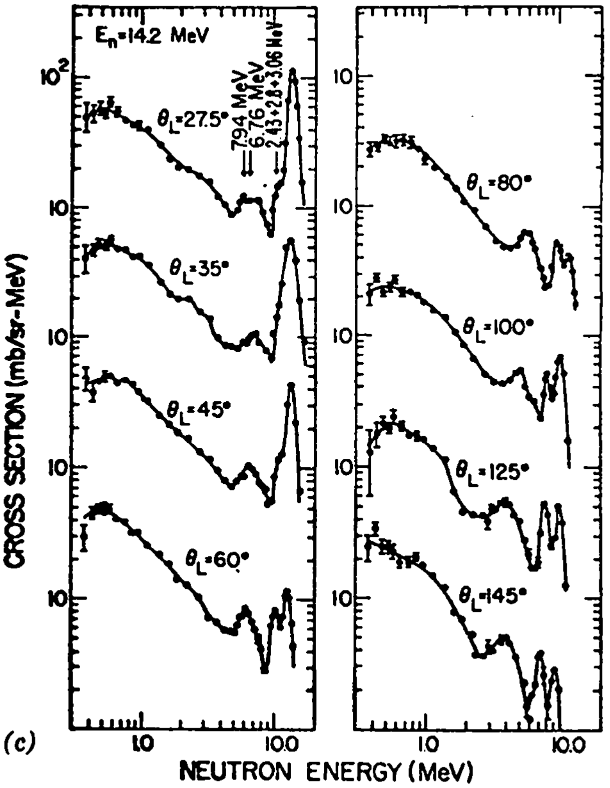

Fig. 3.

Double-differential cross sections for (a) 5.9-MeV, (b) 10.1-MeV, and (c) 14.2-MeV incident neutrons on beryllium. The cross sections are given in the laboratory system. The arrows indicate the positions of the low-lying states in ^{9}*Be, which may contribute to the observed maxima in the cross sections at the indicated energies. In Fig. 3(a) the low-energy shoulder on the elastic peak at* $\Theta_L = 125°$ *is due to poor bunching of the charged particle beam.*

TABLE I

BERYLLIUM DIFFERENTIAL NEUTRON CROSS SECTIONS

E_n	5.9 MeV		10.1 MeV		14.2 MeV	
θ_L	Elastic (mb/sr)	Inelastic ("2.43-MeV" state) (mb/sr)	Elastic (mb/sr)	Inelastic ("2.43-MeV" state) (mb/sr)	Elastic (mb/sr)	Inelastic ("2.43-MeV" state) (mb/sr)
25°	443 ± 57	80 ± 13	480 ± 62	68 ± 14		
27.5°					388 ± 43	
30°					335 ± 37	
35°	320 ± 42	65 ± 11	285 ± 37	49 ± 10	234 ± 26	
45°	180 ± 23	57 ± 10	151 ± 20	43 ± 9	119 ± 13	
60°	75 ± 10	42 ± 7	40 ± 5	35 ± 7	31.1 ± 3.4	18.4 ± 5.5
80°	23 ± 3.1	32 ± 5	15 ± 2.0	26 ± 5.2	11.5 ± 1.3	14.2 ± 4.6
100°	26 ± 3.4	28 ± 4.8	24 ± 3.1	22 ± 4.4	23.0 ± 2.5	13.8 ± 4.1
110°	32 ± 4.0	30 ± 5.2				
125°	31 ± 4.0	28 ± 4.7	15 ± 2.0	26 ± 5.2	9.5 ± 1.1	9.9 ± 3.0
145°					5.7 ± 0.7	7.9 ± 2.4

TABLE II

BERYLLIUM DOUBLE-DIFFERENTIAL CONTINUUM CROSS SECTIONS FOR E_n = 5.9 MeV (mb/sr/MeV)

	θ_L							
ΔE_n (MeV)	25°	35°	45°	60°	80°	100°	110°	125°
0.4 - 0.5	108 ± 16	103 ± 15	99 ± 15	82 ± 12	70 ± 11	45 ± 7	42 ± 6	34 ± 5
0.5 - 0.6	93 ± 14	88 ± 13	82 ± 12	69 ± 10	53 ± 8	37 ± 6	38 ± 6	29 ± 4.3
0.6 - 0.7	83 ± 12	72 ± 10	69 ± 10	49 ± 7	33 ± 4	22 ± 2.8	19 ± 3.0	18 ± 2.3
0.7 - 0.8	69 ± 9	67 ± 9	64 ± 8	43 ± 6	30 ± 4	19.2 ± 2.5	17 ± 2.2	17 ± 2.2
0.8 - 0.9	53 ± 7	56 ± 7	50 ± 7	36 ± 4	27 ± 3	19.0 ± 2.5	16 ± 2.1	19 ± 2.5
0.9 - 1.0	43 ± 5	44 ± 5	40 ± 5	36 ± 4	27 ± 3.2	15.5 ± 1.9	14 ± 1.8	14 ± 1.7
1.0 - 1.25	39 ± 5	35 ± 4	33 ± 4	26 ± 3.1	18.7 ± 2.2	12.3 ± 1.5	11 ± 1.4	11 ± 1.3
1.25 - 1.5	36 ± 4	31 ± 4	25.6 ± 3.1	21 ± 2.5	15 ± 1.8	11 ± 1.3	12 ± 1.4	10 ± 1.2
1.5 - 1.75	32 ± 4	27 ± 3	23 ± 2.7	18 ± 2.1	15 ± 1.8			
1.75 - 2.0	29.5 ± 3.5	24 ± 2.9	22 ± 2.6	17 ± 2.0				

inelastic distributions. The n,2n cross sections are computed assuming that all inelastic processes emit two neutrons. The n,α and the n,t cross sections are taken from the ENDF/B-IV beryllium cross-section library.[11]

V. DISCUSSION

A. Self-Consistency Checks

The cross sections were checked for self-consistency in the following ways. The multiple scattering corrections were checked by taking data with

TABLE III

BERYLLIUM DOUBLE-DIFFERENTIAL CONTINUUM CROSS SECTIONS FOR $E_n = 10.1$ MeV (mb/sr/MeV)

	θ_L						
ΔE_n (MeV)	25°	35°	45°	60°	80°	100°	125°
0.4 - 0.5	61 ± 12	63 ± 12	55 ± 10	47 ± 7.5	36 ± 5.8	24 ± 4.6	23 ± 6.5
0.5 - 0.6	63 ± 9.5	68 ± 10	58 ± 8.7	48 ± 7.2	34 ± 5.1	27 ± 5.7	24 ± 5.0
0.6 - 0.7	63 ± 6.9	66 ± 8.6	54 ± 7.0	48 ± 6.2	29 ± 4.6	28 ± 5.3	23 ± 3.7
0.7 - 0.8	61 ± 79	61 ± 7.9	50 ± 6.5	44 ± 5.7	26 ± 3.4	28 ± 3.6	22 ± 4.0
0.8 - 0.9	57 ± 6.8	51 ± 6.1	44 ± 5.3	39 ± 4.3	23 ± 2.8	25 ± 3.2	20 ± 3.0
0.9 - 1.0	51 ± 6.1	42 ± 5.0	37 ± 4.4	34 ± 3.7	21 ± 2.3	20 ± 2.2	19 ± 2.3
1.0 - 1.25	42 ± 4.6	33 ± 3.6	29 ± 3.2	27 ± 3.0	18 ± 2.0	17 ± 2.4	15 ± 1.7
1.25 - 1.5	32 ± 3.5	27 ± 3.0	25 ± 2.7	21 ± 2.3	16 ± 1.8	13 ± 1.4	13 ± 1.4
1.5 - 1.75	26 ± 2.9	24 ± 2.6	22 ± 2.4	18 ± 2.0	14 ± 1.5	11 ± 1.2	10 ± 1.1
1.75 - 2.0	22 ± 2.4	21 ± 2.3	17 ± 1.9	16 ± 1.8	12 ± 1.3	8.9 ± 1.0	8.0 ± 0.9
2.0 - 2.5	22 ± 2.4	18 ± 2.0	15 ± 1.7	14 ± 1.5	9.5 ± 1.0	6.2 ± 0.7	5.3 ± 0.6
2.5 - 3.0	25 ± 2.7	19 ± 2.1	11 ± 1.2	12 ± 1.3	6.8 ± 0.7	4.4 ± 0.5	3.7 ± 0.4
3.0 - 4.0	20 ± 2.2	14.4 ± 1.6	7.3 ± 0.8	7.5 ± 0.8	4.5 ± 0.5	3.3 ± 0.4	2.2 ± 0.3
4.0 - 5.0	13 ± 1.4	9.1 ± 1.0	5.5 ± 0.6	5.6 ± 0.6			16 ± 2
5.0- 6.0	11 ± 1.2						

TABLE IV

BERYLLIUM DOUBLE-DIFFERENTIAL CONTINUUM CROSS SECTIONS FOR $E_n = 14.2$ MeV (mb/sr/MeV)

	θ_L							
ΔE_n (MeV)	27.5°	35°	45°	60°	80°	100°	125°	145°
0.4 - 0.5	55 ± 10	55 ± 9	44 ± 8	44 ± 7	29 ± 4.4	23 ± 3.5	17.5 ± 3.3	23 ± 3.9
0.5 - 0.6	59 ± 9	53 ± 8	46 ± 7	46 ± 6	33 ± 4.3	22 ± 3.1	20.0 ± 3.2	22 ± 3.7
0.6 - 0.7	58 ± 8	48 ± 6	45 ± 6	39 ± 5	32 ± 4.5	21 ± 2.3	19.5 ± 2.7	19 ± 2.8
0.7 - 0.8	51 ± 6	45 ± 5	44 ± 5	37 ± 4.4	29 ± 3.8	20 ± 2.4	16.5 ± 2.3	18 ± 2.5
0.8 - 0.9	44 ± 5	42 ± 5	40 ± 5	31 ± 3.7	27 ± 3.5	20 ± 2.4	16.0 ± 2.1	17 ± 2.2
0.9 - 1.0	42 ± 5	39 ± 4	36 ± 4	30 ± 3.3	24 ± 2.6	18 ± 2.0	15.5 ± 1.9	16 ± 2.1
1.0 - 1.25	37 ± 4	32 ± 4	29 ± 3.2	24 ± 2.6	18.5 ± 1.9	14.5 ± 1.5	13.5 ± 1.5	13 ± 1.4
1.25 - 1.50	30 ± 3.3	26 ± 2.9	25 ± 2.8	21 ± 2.3	15.5 ± 1.6	13.5 ± 1.4	12.0 ± 1.3	11 ± 1.2
1.50 - 1.75	23 ± 2.5	20 ± 2.2	20 ± 2.2	17 ± 1.9	13.0 ± 1.3	10.0 ± 1.1	8.5 ± 0.9	8.7 ± 1.0
1.75 - 2.0	20 ± 2.2	20 ± 2.2	18 ± 2.0	14 ± 1.5	11.5 ± 1.2	8.3 ± 0.9	6.4 ± 0.8	7.5 ± 0.9
2.0 - 2.5	19 ± 1.3	18.5 ± 2.2	16.5 ± 1.8	13 ± 1.4	9.0 ± 1.0	6.3 ± 0.7	5.2 ± 0.6	5.6 ± 0.6
2.5 - 3.0	18 ± 2.0	14.5 ± 1.7	13.5 ± 1.5	10.5 ± 1.2	7.0 ± 0.8	5.0 ± 0.6	4.2 ± 0.5	4.0 ± 0.5
3.0 - 4.0	15 ± 1.7	11.0 ± 1.3	10.2 ± 1.1	8.0 ± 0.9	4.8 ± 0.5	4.1 ± 0.4	3.9 ± 0.4	4.4 ± 0.5
4.0 - 5.0	11.3 ± 1.2	80 ± 1.0	7.4 ± 0.8	5.6 ± 0.6	4.6 ± 0.5	4.6 ± 0.5	3.7 ± 0.4	4.1 ± 0.5
5.0 - 6.0	9.7 ± 1.1	8.1 ± 1.0	7.8 ± 0.9	6.3 ± 0.7	6.4 ± 0.7	4.3 ± 0.5	2.6 ± 0.3	2.0 ± 0.2
6.0 - 7.0	10.7 ± 1.2	9.2 ± 1.1	8.7 ± 0.6	7.0 ± 0.8	6.4 ± 0.7	4.2 ± 0.5	2.2 ± 0.3	
7.0 - 8.0	10.7 ± 1.2	9.0 ± 1.1	8.0 ± 0.9	5.2 ± 0.6	4.5 ± 0.5	2.9 ± 0.3		
8.0 - 9.0	10.7 ± 1.2	8.0 ± 1.0						

TABLE V

BERYLLIUM ANGLE-INTEGRATED NEUTRON CROSS SECTIONS

Incident Neutron Energy (MeV)	σ_{el}(n,n) (mb)	σ_{inel}(n,n') (2.43-MeV state) (mb)	σ_{inel}(n,n') (continuum) (mb)	σ(n,2n) (mb)	σ(n,α)[a] (mb)	σ(n,t) (mb)	σ(total) (mb)
5.9	1146 ± 149	470 ± 80	654 ± 94	562 ± 62	50	0	1758 ± 161
10.1	1021 ± 133	341 ± 68	764 ± 115	552 ± 67	20	0	1593 ± 149
14.2	995 ± 109	199 ± 64	967 ± 145	583 ± 80	10	18	1606 ± 135

[a] ENDF/B-IV.[11]

samples of different inner radii. The elastic and inelastic cross sections obtained agreed to within 3% and the continuum cross sections to within 10%. The elastic cross sections obtained with the ^{1}H(t,n)^{3}He and ^{3}H(p,n)^{3}He reactions at 5.9 and 10.1 MeV agreed to better than 4%. The statistics on the continuum ^{3}H(p,n)^{3}He data were very poor, and therefore no meaniful comparison could be made with the ^{1}H(t,n)^{3}He data.

Instead of normalizing the elastic data to the n,p cross section using the neutrons scattered from polyethylene, the detector was rotated to 0° to measure the relative neutron flux directly. This allowed the elastic cross section at forward angles to be calculated without relying on the scattering from polyethylene or on the relative efficiency shape. Comparison of the cross sections computed this way with the cross sections computed by using the n,p cross section showed agreement to 3%.

B. Data Comparison

In Fig. 4 the present differential elastic cross sections (circles) for 5.9-, 10.1-, and 14.2-MeV incident neutron energies are compared with the ENDF/B-IV beryllium cross sections (triangles).[11] They are plotted as a function of the cosine of the laboratory scattering angle. The total errors are plotted for each data point. The data agree with the evaluated cross sections within the experimental errors.

Our angle-integrated cross sections are compared in Table VI with the ENDF/B-IV cross sections and with a recent measurement of the n,2n cross sections by Veeser.[12] The agreement among the three sets of n,2n cross sections is good considering that all n,2n cross sections were measured by the integral technique, which counts both neutrons in a large liquid scintillator tank, whereas we measured the energy-angular distributions separately and integrated them to obtain our n,2n cross sections.

The paucity of neutron energy distribution data on beryllium at the incident energies and angles considered in this report, except perhaps at approximately 14 MeV, makes it difficult to make extensive comparisons. At 14 MeV there are two sets of data—that of Prud'homme et al.[13] who measured energy-angular distributions for 14.7-MeV incident neutrons from 0.5 to 7 MeV at scattering angles of 45° and 90°, and that of Hermsdorf et al.[14] who covered the secondary neutron energy range from 2 to 14 MeV at angles of 52.9°, 77.7°, 89.8°, and 131.1° for 14.6-MeV neutrons. If we ignore the slight differences in the incident neutron energies between our data and these two sets of data and linearly interpolate angle in our data tables, we can then make a comparison. This comparison is shown in Fig. 5 for Prud'homme's 45° and 90° data (dashed line), Hermsdorf's 89.8° and 131.1° data (dash-dot line), and our data (solid line). Our data are higher at forward angles and lower than Hermsdorf's data at back angles. However, all three sets are in good agreement at 90°.

For 5.9 and 10.1 MeV there are essentially no continuum energy distribution data. Because most fusion reactor calculations use the ENDF/B-IV library cross sections, we thought it instructive to generate energy distributions from these files at 5.9, 10.1, and 14.2 MeV. The ENDF/B-IV distributions are calculated from models for the emission of the first

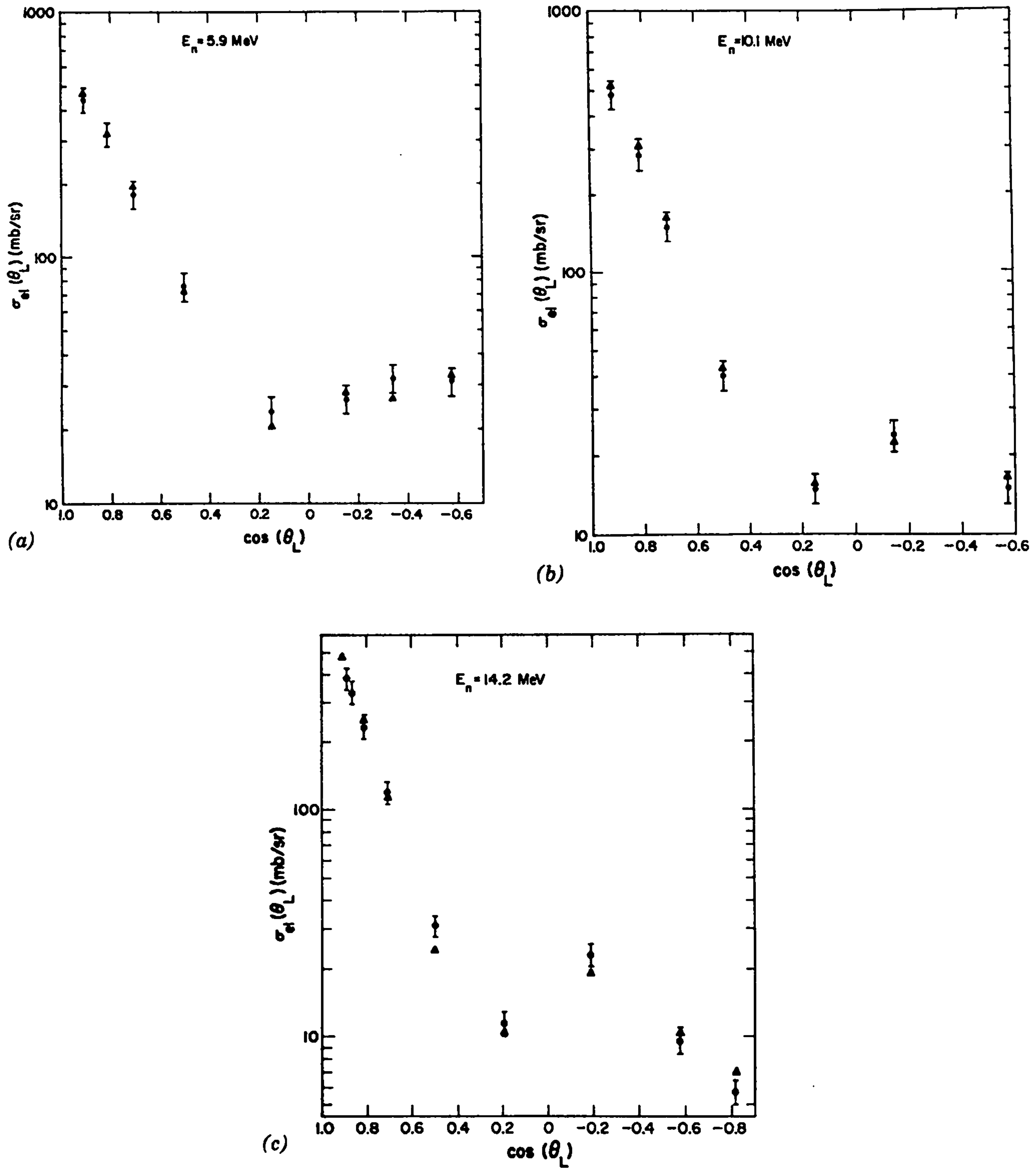

Fig. 4.

Comparison of the present differential elastic cross section (●) and the ENDF/B IV differential elastic cross section (▲) for (a) 5.9-MeV, (b) 10.1-MeV, and (c) 14.2-MeV incident neutrons on beryllium. The laboratory cross sections are plotted as a function of the cosine of the laboratory scattering angle. The total errors are plotted. See text for more details on the errors.

TABLE VI

COMPARISON OF BERYLLIUM NEUTRON CROSS SECTIONS

Incident Neutron Energy (MeV)	$\sigma_{el}(n,n)$ present (mb)	$\sigma_{el}(n,n)$ ENDF/B-IV[a] (mb)	$\sigma(n,2n)$ present (mb)	$\sigma(n,2n)$ ENDF/B-IV[a] (mb)	$\sigma(n,2n)$ Veeser[b] (mb)	σ(total) present (mb)	σ(total) ENDF/B-IV[a] (mb)
5.9	1146 ± 149	1180	562 ± 62	560	576 ± 41	1758 ± 161	1817
10.1	1021 ± 133	1070	552 ± 67	555		1593 ± 161	1660
14.2	995 ± 109	925	583 ± 80	510	482 ± 39 (14.7 MeV)	1606 ± 135	1478

[a] Reference 11.
[b] Reference 12.

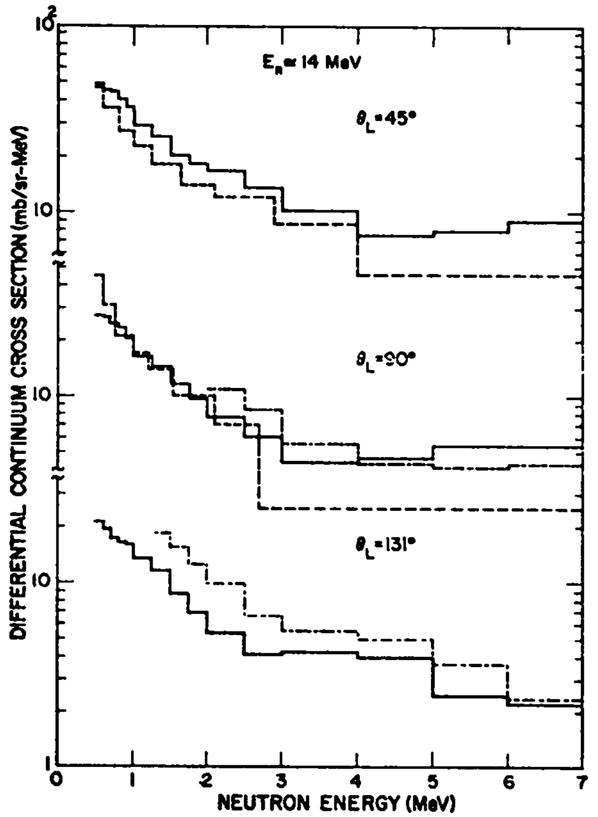

Fig. 5.

Comparison of beryllium double-differential cross sections for approximately 14-MeV neutrons at laboratory angles of 45°, 90°, and 131°: our data (14.2 MeV) solid line, Prud'homme et al.[13] (14.7 MeV) dashed line, and Hermsdorf et al.[4] (14.6 MeV) dash-dot line.

and second neutrons, assuming that the inelastic reaction emits two neutrons. The energy resolution of our experiment was folded into these spectra. Three spectra are compared with our data at laboratory angles of 80° (5.9 MeV), 45° (10.1 MeV), and 125° (14.2 MeV) in Fig. 6. The ENDF/B-IV data are represented by the short and long dash lines and our data by the solid lines. The calculations made at other angles show the same characteristic—that the low-lying states in ^{9}Be are overemphasized in the ENDF/B-IV cross-section library.

At the other extreme is a purely statistical phase space calculation that completely ignores the excited states of a nucleus. Such a phase space calculation is sometimes useful in predicting the energy distribution of the particles from a three- or more-body final state configuration. We calculated the relative neutron energy distribution for the three-body final state configuration consisting of two neutrons and the ^{8}Be nucleus for our incident neutron energies and angles. Some of these results are plotted in Fig. 6 (dashed lines). An arbitrary normalization factor has been applied to these curves for ease of comparison with our data. Clearly the phase space calculation oversimplifies the neutron production mechanism in beryllium by failing to account for the maxima in the cross sections that correspond to transitions to states in ^{9}Be.

The ENDF/B-IV results and phase space calculations show the difficulties inherent in calculating emitted spectra from models and emphasize the

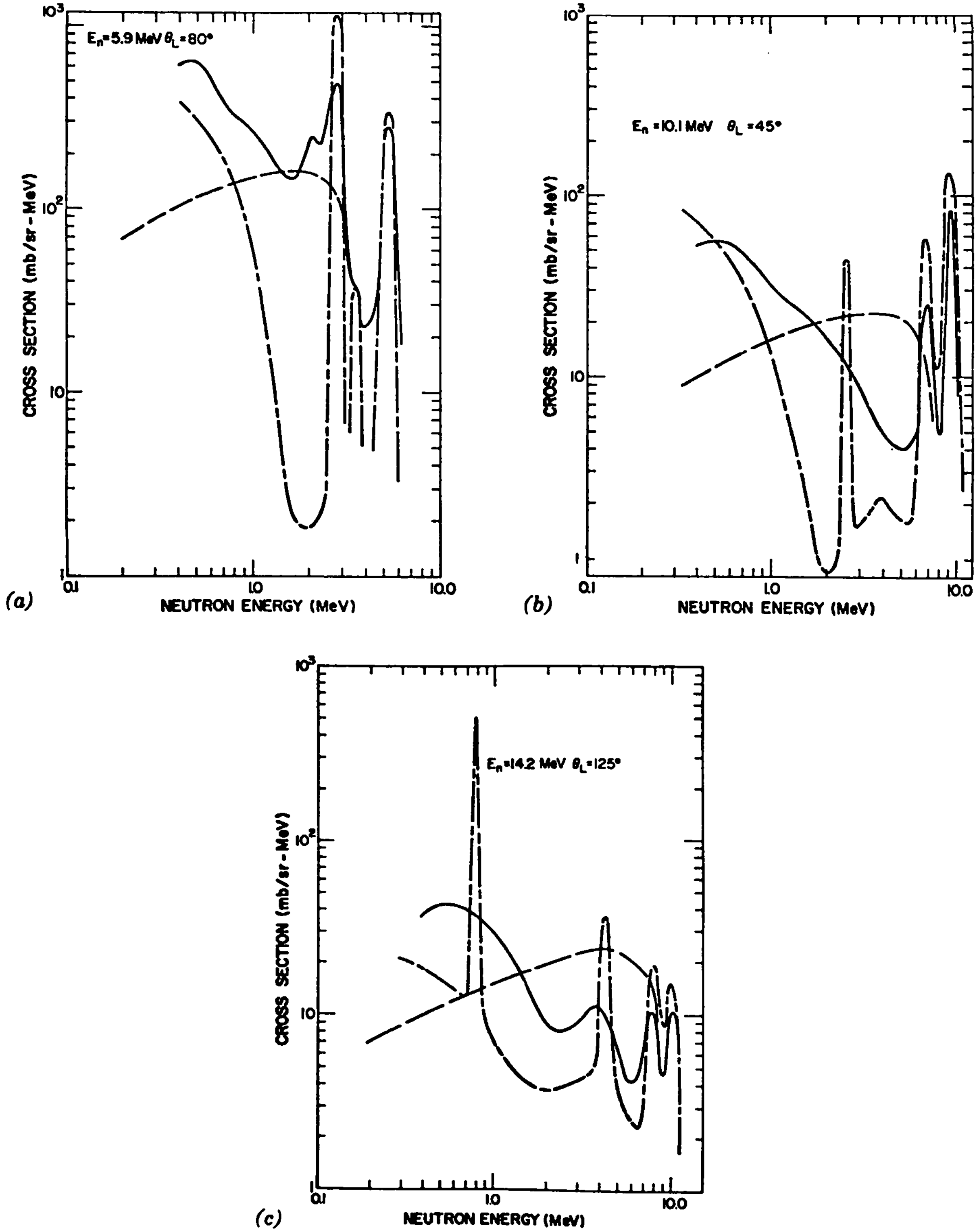

Fig. 6.

Comparison of beryllium double-differential cross sections for a laboratory angle of (a) 80°, (b) 45°, and (c) 125° and an incident neutron energy of (a) 5.9, (b)10.1, and (c) 14.2 MeV. Our data are plotted as a solid line, the ENDF/B data as a short and long dash line, and the unnormalized four-body phase space calculation as a dashed line.

strong need for supporting measurements that determine such spectra. This need is particularly important when the material is a prime component in the structure of any fusion reactor design.

VI. ACKNOWLEDGMENTS

We would like to thank David Turner of the Los Alamos Scientific Laboratory for his help and guidance in setting up the Monte Carlo calculations.

REFERENCES

1. M. Drosg, G. F. Auchampaugh, and F. Gurule, "Signal-to-Background Ratio for Neutron Production between 10 and 14 MeV by the Reactions $^3H(p,n)^3He$, $^1H(t,n)^3He$, and $^2H(d,n)^3He$," Los Alamos Scientific Laboratory report (to be issued).

2. L. Cranberg, R. A. Fernald, F. S. Hahn, and E. F. Shrader, "Production of High-Intensity Ion Pulses of Nanosecond Duration," Nucl. Instrum. Methods **12**, 335 (1961).

3. D. M. Drake, E. D. Arthur, and M. G. Silbert, "Fourteen-MeV, Neutron-Induced Gamma-Ray Production Cross Sections," Los Alamos Scientific Laboratory report LA-5662-MS (1974).

4. N. W. Hill, J. W. T. Dabbs, H. Weaver, "Optimized Detection of Fission Neutrons with Large Liquid Scintillators," Physics Division Annual Progress Report, ORNL-4937 (1973).

5. T. K. Alexander and F. S. Goulding, "An Amplitude-Insensitive System that Distinguishes Pulses of Dependent Shapes," Nucl. Instrum. Methods **13**, 244 (1961).

6. H. Liskien and A. Paulsen, "Neutron Production Cross Sections and Energies for the Reactions $T(p,n)^3He$, $D(d,n)^3He$, and $T(d,n)^4He$,"Nucl. Data Tables **11**, 569 (1973).

7. ENDF/B-IV, Hydrogen data file available on tape as MAT 1269, distributed by Brookhaven National Laboratory (1974).

8. E. D. Cashwell, J. R. Neergaard, W. M. Taylor, and G. D. Turner, "MCN: A Neutron Monte Carlo Code,"Los Alamos Scientific Laboratory report LA-4751 (1972).

9. J. Benveniste, A. C. Mitchell, C. D. Shrader, and J. H. Zenger, "Gamma Rays from the Interaction of 14-MeV Neutrons With Beryllium," Nucl. Phys. **19**, 52 (1960).

10. G. C. Wick, "A Theorem on Cross Sections," Phys. Rev. **75**, 1459 (1949).

11. ENDF/B-IV, Beryllium data file available on tape as MAT 1289, distributed by Brookhaven National Laboratory (1974).

12. L. Veeser, Los Alamos Scientific Laboratory, private communication (1976).

13. J. T. Prud'homme, I. L. Morgan, J. H. McCrary, J. B. Ashe, and O. M. Hudson, Jr., "A Study of Neutrons and Gamma Rays for Neutron-Induced Reactions in Several Elements," Air Force Special Center report AFSWC-TR-60-30 (1960).

14. D. Hermsdorf, A. Meister, S. Sassenoff, D. Seelyer, K. Seidel, and F. Shakin, "Differentielle Neutronenemissionsgvershnitte $\sigma_{nM}(E_o;E,D)$ bei 14.6 MeV Einschus-energie für Elemente Be, C, Na, Mg, Al, Si, P, S, Ca, Ti, V, Cr, Mn, Fe, Co, Ni, Cu, Zn, Ga, Se, Br, Zr, Nb, Cd, In, Sn, Sb, I, Ta, N, Au, Hg, Pb, und Bi," Zentralinstitut für Kernforschung report ZFK-277 (1974).